PAPER

Autonomous shock sensing using bi-stable triboelectric generators and MEMS electrostatic levitation actuators

To cite this article: Mohammad Mousavi et al 2021 Smart Mater. Struct. 30 065019

View the <u>article online</u> for updates and enhancements.

IOP Publishing Smart Materials and Structures

Smart Mater. Struct. 30 (2021) 065019 (13pp)

https://doi.org/10.1088/1361-665X/abf72c

Autonomous shock sensing using bi-stable triboelectric generators and MEMS electrostatic levitation actuators

Mohammad Mousavi, Mohammad Alzgool and Shahrzad Towfighian*

Binghamton University, 4400 Vestal Parkway E., Binghamton, NY 13902, United States of America

E-mail: stowfigh@binghamton.edu

Received 26 January 2021, revised 30 March 2021 Accepted for publication 12 April 2021 Published 11 May 2021



Abstract

This work presents an automatic threshold shock-sensing trigger system that consists of a bi-stable triboelectric transducer and a levitation-based electrostatic mechanism. The bi-stable mechanism is sensitive to mechanical shocks and releases impact energy when the shock is strong enough. A triboelectric generator produces voltage when it receives a mechanical shock. The voltage is proportional to the mechanical shock. When the voltage exceed a certain level, the initially pulled-in microelectromechanical system (MEMS) switch is opened and can disconnect the current in a safety electronic system. The MEMS switch combines two mechanisms of gap-closing (parallel-plate electrodes) with electrostatic levitation (side electrodes) to provide bi-directional motions. The switch is initially closed from a small bias voltage on the gap-closing electrodes. The voltage from the bi-stable generator is connected to the side electrodes. When the shock goes beyond a threshold, the upward force caused by the side electrodes on the switch becomes strong enough to peel off the switch from the closed position. The threshold shock the system can detect is tunable using two control parameters. These two tuning parameters are the axial force on the bi-stable system (clamped-clamped beam) and the bias voltage on the MEMS switch (gap-closing electrodes). The actuation in macro-scale is thus directly connected to a sensor-switch mechanism in micro-scale. This chain makes an autonomous actuation and sensing stand-alone system that has potential application on air bag deployment devices and powerline protection systems. We provide a theoretical frame work of the entire system validated by experimental results.

Keywords: MEMS, triboelectric, nonlinear response, electrostatic levitation, tunability, shock sensing

(Some figures may appear in colour only in the online journal)

1. Introduction

Sensors with no main power source are considered a big step forward because they can be integrated into systems without limitation on size [1], as for passive sensors used for wireless

* Author to whom any correspondence should be addressed.

sensing of body temperature [2], gas concentration [3], and in satellites [4]. Although the sensing part does not need any external driving power, the measurement requires complicated circuitry and digital signal processing to enhance the signal-to-noise ratio [5]. So, more attention is turned toward energy harvesting elements that can be incorporated into the system. Some methods to harvest energy are solar energy through solar cells [1], light through photo voltaic cells [6], mechanical

strain through piezoelectric materials [7–10], thermal energy through thermo-electric units [11], and mechanical impact and friction using triboelectric generators [12–22]. The advancement in energy harvesting mechanisms enables stand-alone sensors, more commonly known as autonomous systems.

Many studies have built autonomous systems by combining an energy-harvesting mechanism with a sensing mechanism [6, 9-11, 20, 21]. The energy from harvesters has been used for different sensing purposes such as carbon dioxide sensors [6], health monitoring [20], biomedical implant monitoring [23, 24], air flow velocity and temperature measurements [10], and security systems [21]. The design of each sensor is influenced by output provided from the energy harvester; some designs incorporate supercapacitors to store the energy [8, 20], some have continuous power [6, 11], and others are triggered by pressure and deformation as in gesture detection [1, 13, 17, 19], wearable electronics [1, 12, 13, 20], and flow [9, 16, 20]. The choice of energy harvester type depends on the power required to operate. For sensors triggered by pressure or deformation, piezoelectric and triboelectric generators are the most common, though they differ in their voltage-current characteristics and power density per mass [25].

A comparison between piezoelectric and triboelectric nanogenerators has proven the superiority of the triboelectric mechanism [25]. The study showed that triboelectric nanogenerators have greater energy density per mass and, unlike piezoelectric ones, they produce high voltage at low frequency. Numerous studies have been conducted on triboelectric nanogenerators for their ability to harvest mechanical energy. They have been used as power sources for different applications such as biomedical implant load sensors [23, 26], motion and gesture detection [12, 13, 17, 19], and ion-concentration measurement [16]. Many material pairs that show the triboelectric property including poly (3,4ethylenedioxythiophene) polystyrene sulfonate and silicone rubber [12], Silicone rubber and steel [13], copper and polytetrafluoroethylene [17], fluorinated ethylene propylene and natural latex [19], polydimethylsiloxane with silver nanowires [20], and polydimethylsiloxane with aluminum [27]. Triboelectric generators are shaped according to the application. For instance; a rotary shape fixed on a motor controls the jetting frequency of a printer nozzle [15]; the triboelectric materials were formed into fabric-shaped units that can be tailored into any wearable shape [13]; triboelectric generator formed like a keypad button to harvest energy from typing motion [17]; and the triboelectric generator is shaped like eyeglasses chassis to serve the object of detecting eye motion [19]; and in [16], rotary disk-shaped triboelectric generator is used to detect water flow. Despite the high energy density of triboelectric generators, their impedance causes difficulty for the matching sensing circuitry. This disadvantage though becomes a useful feature when combining with high voltage electrostatic levitation actuator that we developed in our group [28].

Recently, the attention to switches with levitation actuators has risen because of its advantages over the conventional parallel-plate switches, specifically, the increased travel range and the elimination of pull-in instability of parallel-plate. The conventional way of levitation in micro-electro-mechanical systems (MEMSs) is thermal [29–32]. Adding side electrodes to conventional gap-closing electrodes electrostatically levitates a movable electrode with significantly less power than thermal actuators, and this property has inspired research [28, 33–37]. Other large stroke devices were created using comb drive, torsional springs, and a spiral level arm to create out-of-plane motion [36]. Our team presented simulation and experimental results of a system combining parallel-plate and a levitation actuator for fixed-free and fixed-fixed beam configurations [28, 33].

Nowadays, safety systems use micro-accelerometers to measure transportation or automobile shocks. The real-time measurements are sent to an electronic chip programmed for generating command signals for triggering the safety system. The accelerometer measurements are passed through signal processing and if the programmed safety conditions are satisfied, the control unit manipulates the triggering command. In many safety systems based on control units, several sensors are incorporated to increase reliability. In these cases, sensor fusion process is also required. Signal processing, sensor fusion and command signal manipulation takes some time and power. Control units and sensors cause some delay which is considered a shortcoming of electronic circuits and devices. Control units can slow operating speed, the most important factor in safety systems.

This work aims to simplify control units from safety systems with a safe shock-sensing-trigger system that combines three physical phenomena: bi-stable mechanism [38–40], electrostatic levitation, and triboelectric generation. The device is fully passive and independent of programming. The proposed idea consists of a levitation micro-switch that is fed by a triboelectric generator. The generator is a bi-stable mechanism with triboelectric layers that harvest the mechanical shock energy. Compared with a prior work that merged a triboelectric generator with an electrostatic levitation switch [41], we provide tunability by adding a bi-stable system and bias voltage on the middle electrode. This tunability is essential in designing an autonomous shock system that is sensitive to specific shock thresholds.

Section 2 describes the mechanism. Section 3 models the system mathematically. Section 4 sets up the experiment. Section 5 discusses tests of the feasibility of our idea, characterizes, validates, and compares the model with the experiment. Section 6 summarizes the results and the contribution the research makes.

2. Mechanism description

The autonomous shock sensor merges two transducers based on electrostatic levitation and triboelectric generation. One transducer is a levitation-based micro-electromechanical switch introduced in [33, 28]. The switch of interest consists of a micro-cantilever as the movable electrode, a middle electrode at the bottom responsible for the connection process that closes the switch, and two side electrodes one at each side

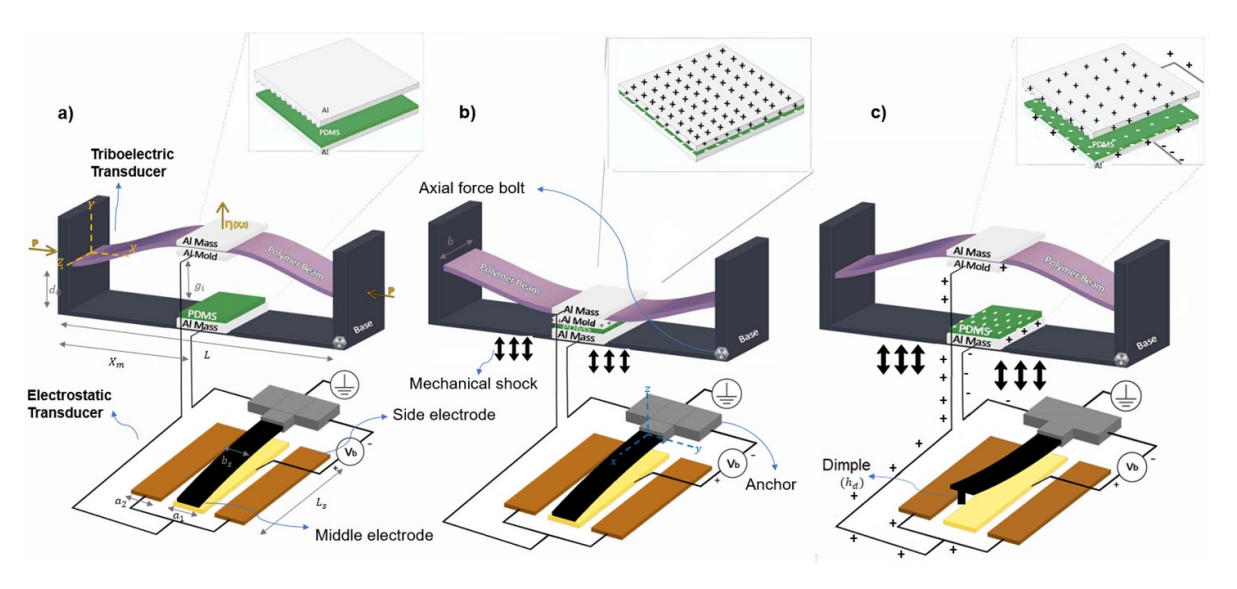


Figure 1. Schematic of autonomous shock sensing system in different stages: (a) before applying the mechanical shock; the triboelectric generator layers are detached and the switch is closed. (b) During the mechanical shock; the triboelectric layers are in contact with each other; the PDMS layer becomes negatively charged; the aluminum layer on top is positively charged, and the switch is still closed. (c) During the mechanical shock; the PDMS layer induces charges to the lower Al layer and the triboelectric layers separate causing a potential difference between the upper and lower Al layers. This potential difference pushes positive charges to the side electrodes and negative charges into the beam causing the fringe filed effect to open the switch.

of the middle electrode that are responsible for the disconnection process. To simplify references, we refer to the voltage applied to side and middle electrodes as the side voltage and middle voltage, respectively. The middle electrode inserts an attractive force on the movable electrode to close the switch, while the side electrodes generate electrostatic levitating force to open it. As the input side voltage vanishes, the attractive force of the middle electrode causes pull-in again. The characterization of the switch was reported in our prior work [41]. Electrostatic levitation means levitating charged objects in an electrostatic field. The process of closing and opening of the switch once the shock goes beyond a certain limit is shown in figure 1. The system includes a triboelectric transducer that is a clamped-clamped polymer beam which buckles under the effect of the axial force P. This force is adjusted using a bolt at the corner of the base. An aluminum electrode is attached to the middle of the beam at the bottom of which a fixed PDMS electrode is attached to the substrate. As a sufficiently large mechanical shock vibrates the base of the structure, the bistable beam switches to the other stable position and hits the PDMS layer. In this process, the kinetic energy of the beam generates an impact where the middle mass hits the triboelectric layer. The impact between the electrodes produces a large open circuit voltage. The generated voltage is desirable for feeding the input of the levitation mechanism which opens the switch (OFF position). Firstly, the switch is in ON position as a result of the pull-in instability. As a mechanical shock occurs the generated voltage at the triboelectric transducer charges the side electrodes and causes the micro-switch to pull-off and switch to OFF position (b). Parts (a) and (b) show the system before and after operation. A schematic shape of dimples is shown in (b). Because the bottom electrode is constantly charged, the movable electrode is usually in the pulled-in, or ON position unless opened by the levitating force. The middle electrode is sustained by a small DC voltage (about 1.5 V). This initial voltage can be provided by a coin battery. The required side voltage is provided by a bi-stable triboelectric transducer. In summary, the triboelectric transducer is a shock-sensitive voltage generator. The produced voltage is sent to a normally-closed MEMS switch. When the shock is strong enough, the trigger actuates and the micro-switch goes to the OFF position.

3. Mathematical modeling

Our mathematical model describes the triboelectric and electrostatic transducers. The first part of the model emulates the triboelectric generator that experiences the environmental shocks and generates the voltage output. The second part simulates the electrostatic transducer that receives the triboelectric voltage and operates the micro-switch. The bi-stable mechanism model contains the mid-plane stretching effect because of the large beam deflection compared to its thickness. In contrast, in the micro-switch cantilever model, there is no mid-plane stretching effect and a Euler-Bernoulli beam theory can predict the beam statics and dynamics [41].

3.1. Part I: triboelectric transducer

As in figure 1, the bi-stable mechanism is a fixed-fixed beam that buckles under the compression of the axial force p making a bi-stable system. We follow the energy approach of a previous work [42] to derive the governing equation describing this

configuration. The relative motion of the continuous system with respect to the base motion is described as:

$$y(X,\hat{t}) = \psi(X) + \phi(X)\eta(\hat{t}) \tag{1}$$

where X, \hat{t} and $y(X,\hat{t})$ stand for the axial position, time, and relative beam motion, respectively. Also, $\psi(X)$ and $\phi(X)$ are the buckled shape and the first mode-shape corresponding to the buckled configuration, respectively. The time function corresponding to the first mode of the buckled configuration is represented by $\eta(t)$. The mode shape is normalized such that $\phi(X_{\text{max}}) = 1$, hence $\eta(t)$ also represents the displacement of the middle mass relative to the buckled configuration $\psi(X_{\text{mid}})$. The final equation of motion will be:

$$M_{1} \frac{\partial^{2} \eta}{\partial \hat{t}^{2}} + D_{1} \frac{\partial \eta}{\partial \hat{t}} + k_{L} \eta + k_{Q} \eta^{2} + k_{C} \eta^{3}$$

$$= -\left(M_{Z} \frac{\partial^{2} z}{\partial \hat{t}^{2}} + \alpha_{1} q + \alpha_{2} q^{2}\right) + F_{D}$$
 (2)

where M_1 = mass coefficient, D_1 = damping coefficient, k_L = linear stiffness, k_Q = quadratic stiffness, k_C = cubic stiffness, M_Z = base excitation mass coefficient. α_1 and α_2 stand for electrical constants. The calculation procedure of the parameters in equation (2) is available in [42]. The transferred charge is denoted by q(t). The impact force F_D between the generator electrodes is modeled [43, 44] as a linear damper and spring as:

$$F_{\rm D} = -c_i \frac{\partial \eta}{\partial \hat{t}} - k_i \eta. \tag{3}$$

 $F_{\rm D}$ in equation (2) is activated when the beam hits the PDMS layer. The values of k_i and c_i are available in table 3. The base-excitation (denoted by z(t)) is assumed to be a motion in Z-direction. The transferred charge between the triboelectric layers is governed by:

$$\frac{\partial q}{\partial \hat{t}} = -\frac{q}{\epsilon_0 SR} \left[\frac{T_{\text{PDMS}}}{\epsilon_r} + d_0 + y(X_{\text{mid}}, \hat{t}) \right] + \frac{\sigma}{\epsilon_0 R} (d_0 + y(X_{\text{mid}}, \hat{t}))$$
(4)

where ϵ_0 , ϵ_r , S, $T_{\rm PDMS}$, σ indicate the vacuum permittivity, relative permittivity, contact area, thickness of the PDMS layer, and surface charge density, respectively. d_0 is the initial gap between the electrodes when there is no axial load. R represents the total electrical resistance in the current path.

3.2. Part II: electrostatic transducer

A micro-cantilever that is subject to the electrostatic fields of one middle electrode charged with V_b and two side electrodes charged with V_s is modeled in this section. The electrostatic forces per unit length $(\hat{f}_e(\hat{w},\hat{x},\hat{t}))$ are expressed using approximation functions obtained from COMSOL simulations. The electrostatic force data is manipulated by calculating the potential energy between each pair of electrodes in the micro-switch configuration (see figure 1).

The micro-switch is fabricated using the PolyMUMPS MEMS standard; the cross-section area, the second moment of area about the *x*-axis, and the material distribution are uniform along the *x*-axis. An Euler-Bernoulli beam equation is used to describe its motion. The Euler-Bernoulli beam model is valid because the length of the micro-beam is much larger than its thickness and the plane section remains plane and perpendicular to the neutral axis. Also, the lateral deflections (maximum of 4 μ m) are yet small compared to the beam length (505 μ m). Thus, the equation of motion for the switch is

$$\rho_s A_s \frac{\partial^2 \hat{w}}{\partial \hat{t}^2} + \hat{c}_s \frac{\partial \hat{w}}{\partial \hat{t}} + E_s I_s \frac{\partial^4 \hat{w}}{\partial \hat{x}^4} = \hat{f}_e(\hat{w}, \hat{x}, \hat{t}). \tag{5}$$

The switch micro-cantilever is considered as a continuous system and the transverse displacement is denoted by $\hat{w}(\hat{x},\hat{t})$. $\hat{w}(\hat{x},\hat{t})+d$ represents the gap between the micro-beam and the substrate. The equation of motion is nondimensionalized (see table 2) and then the first order Galerkin's method is applied to simplify the system partial differential equation to an ordinary differential equation as $w(x,t) = \Phi(x)\nu(t)$ where w,x,t are the nondimensional forms of $\hat{w}, \hat{x}, \hat{t}$. The shape function is obtained by considering a uniform distributed force over the micro-beam as

$$\Phi(x) = C_1 \cos(\lambda x) + C_2 \sin(\lambda x) + C_3 \cosh(\lambda x) + C_4 \sinh(\lambda x)$$
(6)

satisfying the boundary conditions $\Phi(0) = 0$, $\Phi'(0) = 0$, $\Phi''(1) = 0$ and $\Phi'''(1) = 0$. After integration over the length of the beam, the governing ODE was obtained as

$$m\frac{\partial^2 \nu}{\partial t^2} + cm\frac{\partial \nu}{\partial t} + k\nu = F_e(\nu, t) \tag{7}$$

where $\nu(t)$ is Galerkin's time function related to the first mode. $\nu(t)$ represents the nondimensional micro-cantilever tip displacement. The nondimensional electrostatic force per unit length includes three parts as in equation (8)

$$f_e(w,t) = f_{11}(w,t) + f_{12}(w,t) + f_{22}(w)$$
 (8)

where f_{11} represents the electrostatic levitation (repulsive) force

$$f_{11}(w,t) = V_s^2 \sum_{i=0}^9 a_i w^i$$
 (9)

 f_{12} indicates the coupled term from repulsive and attractive forces

$$f_{12}(w,t) = V_s V_b \sum_{i=0}^{9} b_j w^j$$
 (10)

and f_{22} shows the gap-closing electrode (attractive) forces

$$f_{22}(w,t) = V_b^2 \frac{\beta}{(w+1)^{2.15}}. (11)$$

Table 1. Electrostatic force coefficients obtained from COMSOL simulation.

Parameter	Value	Parameter	Value
$\overline{A_0}$	1.84×10^{-3}	B_0	3.21×10^{-3}
A_1	1.38×10^{-4}	B_1	-2.91×10^{-3}
A_2	1.02×10^{-4}	B_2	9.74×10^{-4}
A_3	1.86×10^{-5}	B_3	-2.55×10^{-4}
A_4	-1.27×10^{-6}	B_4	5.43×10^{-5}
A_5	-1.38×10^{-7}	B_5	-8.52×10^{-6}
A_6	3.70×10^{-9}	B_6	8.97×10^{-7}
A_7	-3.29×10^{-9}	B_7	-5.88×10^{-8}
A_8	1.39×10^{-11}	B_8	2.13×10^{-9}
A_9	-2.31×10^{-12}	B_9	-3.33×10^{-11}
β	-0.463	λ	1.875

Using the single order Galerkin's method of discretization, the nondimensional micro-switch tip displacement is approximated by:

$$w(x,t) \approx \Phi(x)\nu(t)$$
. (12)

The nondimensional force term corresponding to equations (13)–(15) is calculated by

$$F_{11} = V_s^2 \sum_{j=0}^9 A_j \nu^j \tag{13}$$

$$F_{12} = V_s V_b \sum_{j=0}^{9} B_j \nu^j \tag{14}$$

$$F_{22} = V_b^2 \frac{\beta}{(\nu+1)^{2.15}}. (15)$$

The values of A_j , B_j , λ and β are indicated in table 1. The effect of the initial curl of the micro beam was not negligible and was considered in the analysis. Using optical imaging the initial beam gap was approximately measured 1 μ m between the cantilever tip and the substrate. This curvature requires higher initial pull-in (middle) voltage than the predicted value using the nominal gap. To reduce the contact area between the movable and the middle electrodes, the micro-cantilever was dimpled at the bottom surface. The dimples restrict the downward motion range to 1.25 μ m. Therefore, the order of magnitude of the initial curl in comparison with the initial gap is not negligible and should be considered in calculations. For this purpose, an average curl of 1 μ m is added to the tip displacement.

4. Experimental setup

The setup is split into two parts: the triboelectric transducer and the electrostatic transducer.

4.1. Part I: triboelectric transducer

This part contains a shock activated generator and triboelectric layers attached to a bi-stable mechanism (see figure 1). The

Table 2. Nondimensionalization of the micro-switch partial differential equation.

Actual value	ND value
Axial position	$x = \frac{\hat{x}}{L_s}$
Beam gap (μm)	$w = \frac{\hat{w}}{d_s}$
Time	$t=rac{\hat{t}}{T}$
Time constant	$T = \sqrt{rac{ ho_s A_s L_s^4}{E_s I_s}}$
Damping coefficient	$c_s = rac{\hat{c}L_s^4}{E_sI_sT}$
Force constant	$r = \frac{L_s^4}{E_s I_s h_s}$

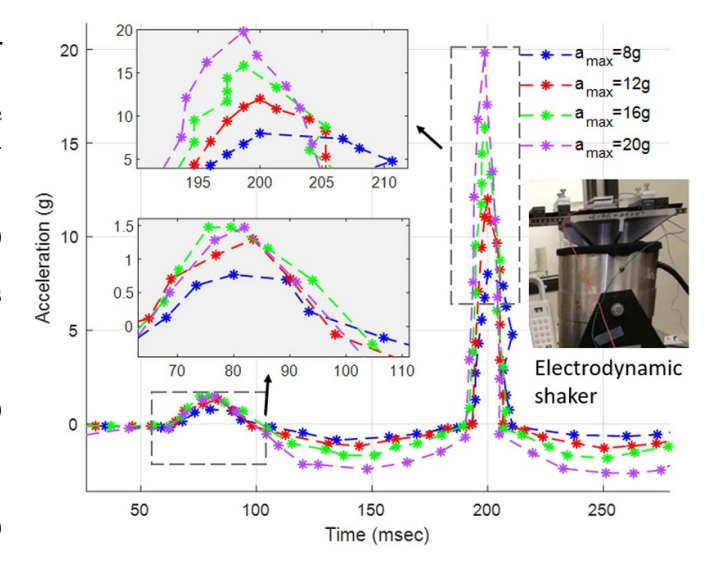


Figure 2. Generator base acceleration with pre-compensation made an electrodynamic shaker driven by PUMA Spectral Dynamics. Various shock powers are indicated with different colors. A PCB piezo-accelerometer was used for the measurements.

base acceleration is controlled by a PUMA Spectral Dynamics mechanical shock simulator that can produce shocks at a variety of powers. Using a closed-loop control system, this machine manipulates an input signal. The input is then amplified (using Techron 5530 Power Supply Amplifier) and applied to an electrodynamic shaker. Two PCB Piezotronics 352A24 accelerators were attached to the bi-stable mechanism for sending measurement and control signals to the Spectral Dynamics system. The input signals received by the electrodynamic shaker are plotted in figure 2. A translation stage was fixed on top of the shaker where the bi-stable mechanism is installed. Considering figure 3, at step 1 the mechanical shock is simulated and as a result, at step 2, a high voltage is generated at the bi-stable mechanism. The generated voltage data is recorded using the oscilloscope real-time data acquisition.

The bi-stable mechanism is a polymer beam fixed at both ends. The design parameters are listed in table 3. A load cell was placed at one of the fixed ends for axial load measurement. Over the bottom surface at the middle of the beam, an aluminum electrode is fixed. Under the aluminum layer, the PDMS layer as the other electrode was fixed on the substrate.

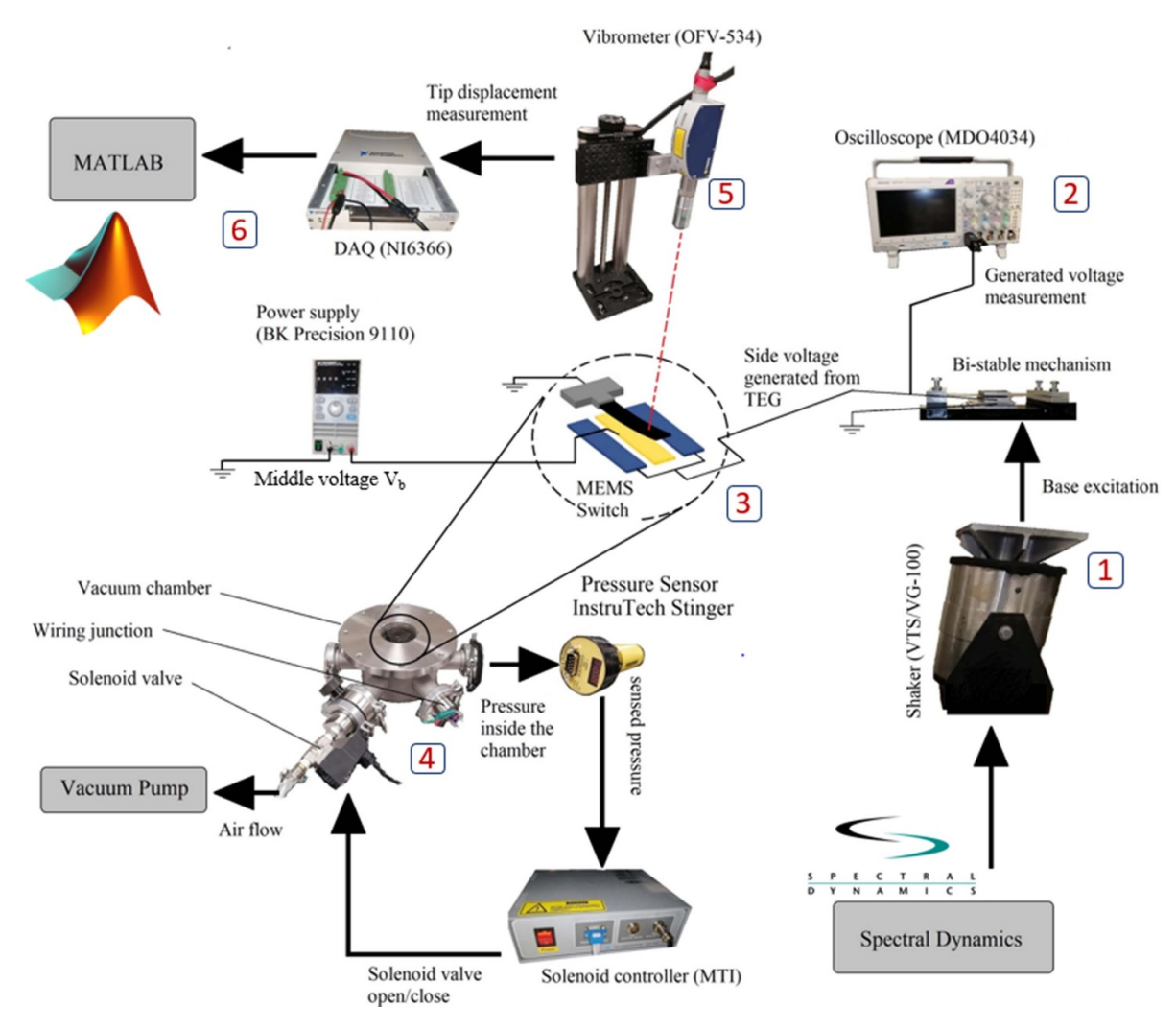


Figure 3. Components of the autonomous shock sensing system. (1) is the electrodynamic shock generator, (2) is the oscilloscope used for recording real-time shock data, (3) is levitation-based micro-switch, (4) is a sealed chamber containing the micro-switch, (5) is the laser vibrometer observing the micro-switch motion and velocity, (6) is the data acquisition system recording the vibrometer measurements.

By applying an axial force p larger than the first critical load, the beam buckles. The direction of the curvature must be in the direction away from the bottom.

4.2. Part II: electrostatic transducer

The micro-cantilever with the special electrode design (figure 1) was fabricated using the PolyMUMPs standard fabrication performed by MEMSCAP. An optical profiler was used to measure the dimensions. The micro-cantilever used in the switch is not straight. The beam tip is curled up as observed by the optical images [28] due to the thermal stress during the fabrication process. The material properties and the design geometry can be found in table 4.

Unless indicated, the experiments were conducted at the atmospheric pressure, at the lab temperature 22 °C, with the relative humidity of 37%. The micro-beam tip displacement and velocity are measured with a laser vibrometer (Polytec MSA-500). The measured data are received and conveyed to MATLAB through a data acquisition system (National

Instruments USB 6366 DAQ). The side voltage is provided by a wide-band amplifier (Krohn-Hite 7600). A DC power supply (B&K Precision 9110) supplies the middle voltage. The order of magnitude of the side voltage is approximately ten times larger than the bias voltage. The variation is caused by different electrostatic fields, i.e. parallel-plate for attraction and fringe field for repulsion at the middle and the side electrodes, respectively. The voltages were manipulated with MATLAB and the outputs are measured by two electrometers (Keithley 6514) and transferred to MATLAB again through the data acquisition system. In figure 3, the generated voltage at step 2 is transferred to the side electrodes of the micro-switch (step 3). The switch motion is measured at step 4. The micro-switch is kept in a chamber for experiments in different pressures (step 5). Finally, all the measurement data is sent to MATLAB for further analysis (step 6). An overall view of the setup in the MEMS and Energy Harvesting Laboratory at Binghamton University can be found in figure 4. The steps marked in figure 3 are also shown in figure 4.

Table 3. Dimensions and properties of the triboelectric transducer.

Symbol	Value
$L \times b \times h_0$	$14 \times 3.6 \times 0.2$ cm
$L_m \times b_m \times h_m$	$3.6 \times 5 \times 0.5$ cm
c	$95 \mathrm{Ns} \mathrm{m}^{-1}$
d_0	1.4 mm
ε_r	$2.5\varepsilon_0$
g_i	$1.3~\mu\mathrm{m}$
E	2.34 GPa
p	30 N
$T_{ m PDMS}$	$300~\mu\mathrm{m}$
ρ	$1220 \mathrm{kg}\mathrm{m}^{-3}$
k_i	$30000 \mathrm{N}\mathrm{m}^{-1}$
c_i	$3000 \mathrm{Ns} \mathrm{m}^{-1}$
	$L \times b \times h_0$ $L_m \times b_m \times h_m$ c d_0 ε_r g_i E p T_{PDMS} ρ k_i

Table 4. Dimensions and properties of the electrostatic transducer.

Parameter	Symbol	Value
Beam length	L_s	505 μm
Beam width	b_s	$20.5~\mu\mathrm{m}$
Beam thickness	h_s	$2 \mu \mathrm{m}$
Module of elasticity	E_s	160 GPa
Density	$ ho_s$	2330 kg m^{-3}
Initial gap	d_s	$2~\mu\mathrm{m}$
Middle electrode width	a_1	$32 \mu m$
Side electrode width	a_2	$28 \mu m$
Electrode thickness	h_1	$0.5~\mu\mathrm{m}$
Dimple height	$h_{ m d}$	$0.75~\mu\mathrm{m}$

5. Results and discussion

In this section, we show and discuss the results of the proposed device including a triboelectric generator and a levitation micro-switch. The simulation results are also compared with the experiments in this section. The experiments were conducted based on the instructions of section 4. The simulation results were obtained using Wolfram Mathematica and MATLAB where the equations of both system components are solved simultaneously.

The characterization starts with investigating the relationship between the shock magnitude and the triboelectric voltage generation, see figure 5. An axial force of p = 30 N was applied to the bi-stable mechanism which buckled the bridge buckled. The shock power was controlled by a PUMA Spectral Dynamics simulator. The bi-stable mechanism absorbs energy from the base-excitation and switches to the other stable equilibrium point. The switching is triggered when the shock power exceeds a threshold i.e. a function of the axial force p. Figure 5 shows that for p = 30 N, the least shock power for producing impact between triboelectric layers is a = 3g. Beyond this limit, there is a transitional region where the generated voltage varies sharply as the shock power is increased (3g < a < 5g). For a > 5g a linear relation is observed between the shock power and the generated voltage. The latter region is ideal for a tunable device.

The bi-stable mechanism provides a 1-dimensional shock sensing. The strength of shock needed to open the switch,

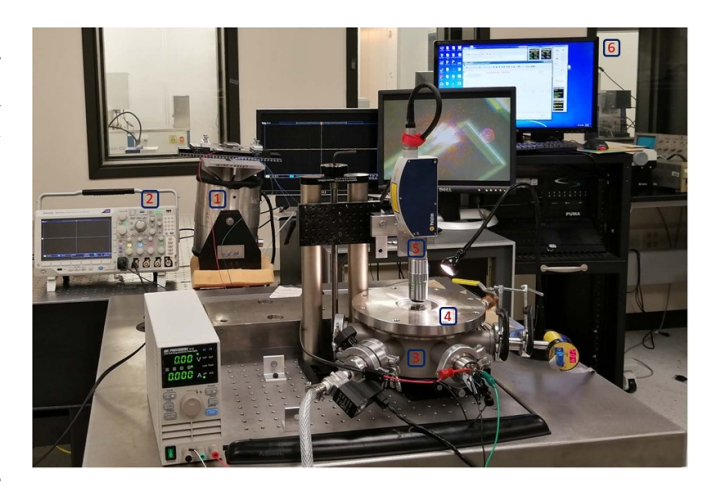


Figure 4. Components of the autonomous shock sensing system. (1) is the electrodynamic shock generator, (2) is the oscilloscope used for recording real-time shock data, (3) and (4) is the vacuum chamber containing the levitation-based micro-switch, (5) is the laser vibrometer observing the micro-switch motion and velocity, (6) is the computer connected to the data acquisition system recording the vibrometer measurements. The numbers labeled beside the component are consistent with figure 3.

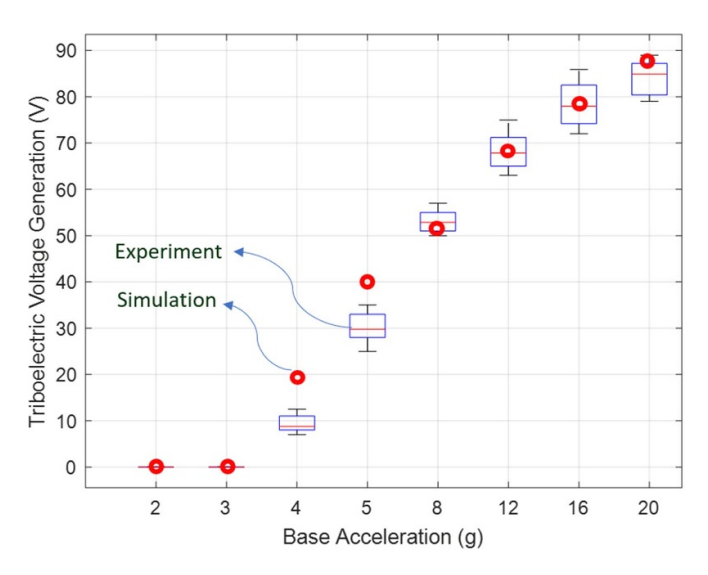


Figure 5. Generator output versus shock power. The box-plots show the results of ten tests for each base acceleration. The horizontal black lines show the range for the generated voltage. The vertical black line shows an average estimation of the measured data. The red circles indicate the simulation results.

is adjustable as the axial force can easily be tuned according to the user's requirement. In the following, we present the results of the generated voltage versus the shock power. The charge density between the triboelectric layers (aluminum and PDMS), is an uncertain parameter as it depends on many factors such as the PDMS thickness, surface roughness, electrode surface pattern, surface alignment. Even for two successive identical tests, the generated voltage may differ significantly. For the experimental result at 12g base-excitation (as a median shock power), the average generated voltage is 63 V and is related to the charge density of $\sigma = 7 \times 10^{-6}$ C m⁻².

The simulation consists of solving the nonlinear bi-stable dynamic equation (2) and solving the triboelectric equation (3). The results are plotted with red circles in figure 5. The simulation error is low in the linear region (a>6g), but deviates for small excitations (3g < a < 5g). The model provides good estimation of the minimum base-acceleration for voltage generation i.e. $a \sim 3g$. The transient region (3g < a < 5g) is hard to predict because the bi-stable mechanism is operating close to its unstable equilibrium point. Moreover, the shock generation is not perfectly done as the shaker may work slightly differently from one test to another. For example, when the command signal was set to achieve a=4g, the following measured outputs were reported 3.85g, 4.15g, 4.22g. Hence, the simulation cannot capture the transient region with good precision.

We estimated both the bi-stable mechanism and the MEMS switch time solutions using Galerkin's reduced order method. First, equation (2) is solved which is inputted with values from the base-excitation signal. Then, the generator motion is transferred to the triboelectric equation. The simulation is followed by transferring the generated voltage (as the side voltage V_s) to the MEMS switch discretized dynamic equation. Damping is an uncertain factor in the bi-stable mechanism. Structural damping c and the damping of the impact model c_i determine how quickly the transient response dissipates. Moreover, those coefficients are important for simulating the magnitude of the generated voltage. The values were chosen from the transient response analysis of the bi-stable mechanism. The damping coefficient also plays an important role during the transient response, while it does not affect on the steady-state response of a switch actuated by DC side and middle voltages. We identified a damping value that can closely predict the dynamics. The damping ratio was identified to be $\zeta = 2.213$ and $\zeta = 28.45$ under P = 4900 mTorr and atmospheric pressure, respectively. These values are acquired by comparing the simulation with experimental results.

To illustrate the switch operation, we use a DC generator and record the switch response (figure 8). In section 4, we showed that the micro-switch mechanism includes a DC source feeding the middle electrode (V_b) so that the movable electrode is initially kept in the pull-in position. This enables us to acquire a normally-closed (ON) micro-switch. The static pull-in was found to be $V_{\rm SPI} = 2.05$ V for the microswitch cantilever i.e. the required middle voltage for initiating pull-in is at $V_s = 0$ V. Compared with the dynamic pullin, static pull-in is used as the required middle voltage in the switch connection process because it gives a more conservative threshold. Then, another source providing a high voltage command signal should be applied to the side electrodes to disconnect the switch by levitating the cantilever. In today's industry, such a signal is manipulated by electronic control units. While in this work, the triboelectric transducer feeds the triggering part (micro-switch) a high-amplitude input voltage autonomously.

As in figure 6, the micro-switch is initially at the pullin position with $V_b = 1.5$ V. At t = 3 s, the side electrodes are charged with $V_s = 65$ V and the micro-switch is released from pull-in (disconnection process). Note that $V_b = 1.5$ V and

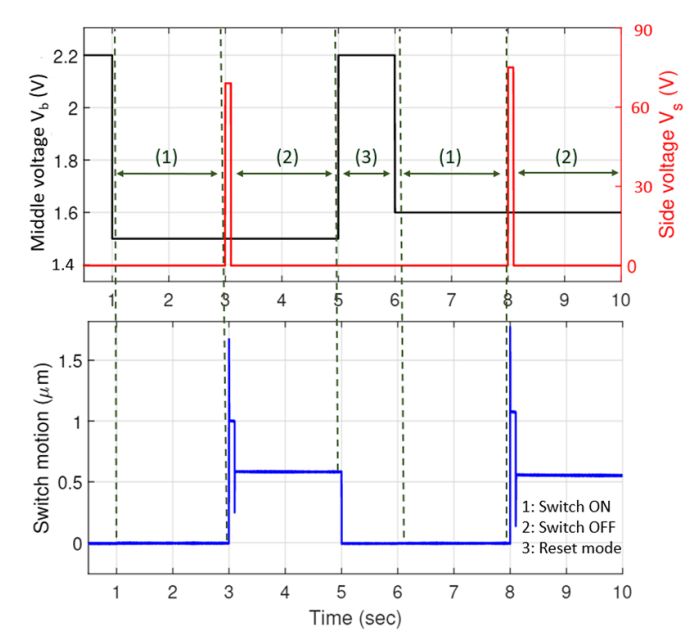


Figure 6. The levitation-based micro-switch operation test at 1 atm. (a) shows the input of the middle and side voltage. The switch motion during the opening and closing processes is demonstrated in (b). The micro-switch operation steps are demonstrated with dashed lines: (1) switch is ON; (2) switch is OFF; (3) the resetting process where a larger middle voltage is applied so that pull-in happens.

 $V_{\rm b} = 1.6 \, \rm V$ are not sufficient for initiating pull-in, because the beam will reach an equilibrium above the substrate. Therefore, once the side voltage vanishes, an auxiliary DC voltage is added in a way that the resultant middle voltage becomes larger than the static pull-in voltage ($V_b > V_{SPI} = 2.05 \text{ V}$). We used $V_b = 2.2 \text{ V}$ for the resetting process in which the microswitch goes to the ON position. The test was repeated with $V_{\rm b} = 1.6$ V. As it is expected, the settled position of the beam is slightly lower as the middle voltage is increased. Damping (pressure) affects the switch rise time and its performance in the transient region, but will not affect its steady-state response. The required side voltage is tunable using the middle (bias) voltage. This tunablity is achieved from the relationship between middle and side voltages for release. In the presence of $V_b = 1.5$ V, the least side voltage for the disconnection process is $V_{\rm s} \sim 75$ V and for $V_{\rm b} = 1.6$ V, the micro-switch requires $V_{\rm s} \sim 80$ V for opening. As mentioned in section 3, the required side voltage in the peel-off process must overcome the attractive force between the electrodes, and the adhesion forces between the involved surfaces.

To demonstrate the release voltage at different bias voltages, we present figure 7 that shows the measured response of the switch at various pressures. We first apply $V_b = 2.5 \text{ V}$ to make sure the switch is in ON position. Then, the middle voltage is reduced to the amount indicated on the horizontal axis. At this stage, we have a pulled-in micro-cantilever. Subsequently, the side voltage increases as a ramp function. At a specific amount called the release voltage, the switch opens and goes to the OFF position. In this figure, The release voltage (vertical axis) corresponding to different middle voltages

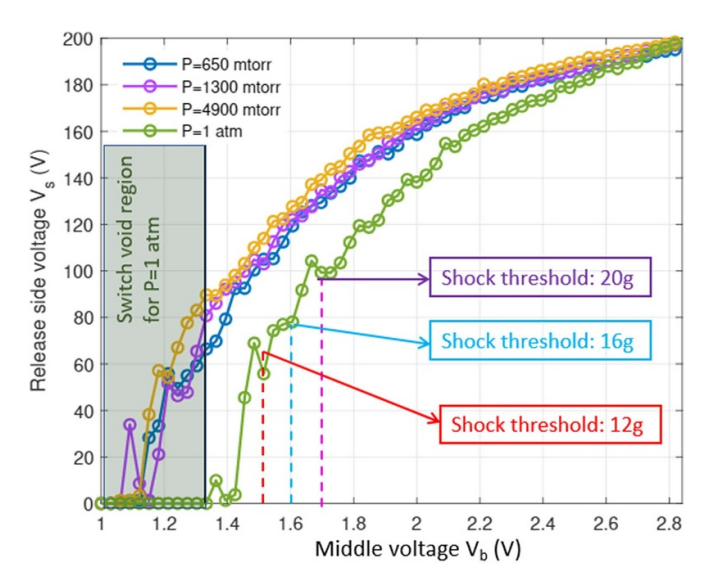


Figure 7. Release diagram of the switch micro-cantilever operating at various pressures. The switch is closed by applying a large middle voltage which is then reduced to the amount indicated on the horizontal axis. The vertical axis shows the recorded amount of side voltage (V_s) to release the switch during the disconnection process. The dashed lines and arrows show the shock threshold corresponding to the specified micro-switch middle voltage at 1 atm. The grey area shows the micro-switch void region where the middle voltage is inadequate to close the switch.

(horizontal axis). At P=1 atm, for $V_b < 1.3$ V, the attractive electrostatic force cannot overcome the spring forces of the switch and the switch stays open. Therefore, the DC source of the middle voltage must be set at $V_b > 1.3$ V. We used $V_b = 1.5$ V, 1.7 V in order that the initial adhesion is guaranteed when the micro-switch is ON. The middle voltage of the connected switch determines the required amplitude of the input voltage V_s . As mentioned in section 4, the input voltage originates from mechanical shocks. Considering three middle voltages $V_b = 1.5$ V, $V_b = 1.6$ V, $V_b = 1.7$ V, the required side voltage for the disconnection process (release) is $V_s \sim 60$ V, $V_s \sim 75$ V, $V_s \sim 90$ V, respectively. Using figure 5, the least shock power for generating such voltages will be a = 12g, a = 16g, a = 20g (see figure 7).

Figures 8–11 demonstrate the operation of the autonomous shock sensing system in the time-domain. With respect to the micro-switch characteristics that vary with the environment pressure, we provided the results for the operation at low pressure (4900 mTorr) and the atmospheric pressure (760 Torr). Regarding the operation at 1 atm, as in figure 7, at $V_b = 1.5 \text{ V}$ and $V_b = 1.7$ V, the required side voltage for releasing the closed switch is $V_s = 60 \text{ V}$ and $V_s = 90 \text{ V}$, which can be generated with the shock strength of a = 12g, a = 20g (see figure 5), respectively. At 4900 mTorr, at $V_b = 1.2 \text{ V}$ and $V_b = 1.4 \text{ V}$, the required side voltage for releasing the closed switch is $V_{\rm s}=60~{\rm V}$ and $V_{\rm s}=90~{\rm V}$, which can be generated with the shock strength of a = 12g, a = 20g, respectively (see figure 5). Therefore, to set the device shock threshold to a = 12g, the micro-switch middle voltage should be adjusted to $V_b = 1.2 \text{ V}$ and $V_b = 1.5 \text{ V}$ for P = 4900 mTorr and P = 1 atm, respectively. The same voltages for the shock threshold of a = 20g should be set to $V_b = 1.4 \text{ V}$ and $V_b = 1.7 \text{ V}$. Figures 8 and 9 show the results of the operation at P=1 atm. As the command signal (figure 2) is sent to the electrodynamic shaker, the generated shock causes the upper electrode of the triboelectric generator to hit the lower electrode (PDMS), and it immediately bounces very slightly. The simulation results at the subfigures (a) and (b) illustrate the velocity and the displacement of the generator upper electrode. The velocity at which the impact occurs is 650 mm s⁻¹ and 980 mm s⁻¹ for a = 12g, a = 20g, respectively. Part (c) shows the generated voltage which is $V_s = 60$ V and $V_s = 90$ V for a = 12g, a = 20g, respectively. As seen in part (c), the generated voltage is much higher than the noise amplitude before and after the shock $(\sim 10 \text{ times})$. A high signal-to-noise ratio is advantageous in sensing devices. The negative part of the generated voltage happens during the separation of the triboelectric layers. Part (d) demonstrates the micro-switch motion that goes to the OFF position during the actuation process and oscillates around the stable equilibrium point corresponding to the micro-switch middle voltage. The simulation and the experimental results are compared in the subfigures (c) and (d). The same results for P = 4900 mTorr are reported in figures 10 and 11.

An important tuning parameter to control the threshold shock of detection is the bias voltage on the middle electrode. The control of bias voltage is an alternative method to adjust this threshold in addition to the change of axial load on the bi-stable system. The axial force on the generator provides a method to adjust the threshold sock for detection. Our results in this paper are obtained for the axial force of p=30 N. At different axial force conditions, there will be a different triboelectric voltage generation. The tunability of the bi-stable triboelectric generator based on the axial force was discussed in [42]. However, tuning the bias voltage on the middle electrode is easier than the axial force because it is based on electrical signals and not the mechanical load on the bi-stable structure.

A monotonic relation exists between the required bias voltage and the threshold shock as shown in figure 12. In this figure, the experimental results measured at four middle voltages $V_b = 1.4, 1.5, 1.6, 1.7 \text{ V}$ are shown. This relatively linear correlation between the sensor shock threshold and the tuning parameter V_h is desirable. As mentioned before, when the micro-switch is in pull-in position, the least middle voltage for keeping the switch ON is $V_b = 1.3$ V. For 1.3 V $< V_b <$ 1.4 V, the micro-switch is over-sensitive to environmental impacts. Even a small acceleration or a tapping can unintentionally make the micro-switch operate. Hence, the workable region is considered as $V_b > 1.4$ V. The graph also shows the results at a reduced pressure of 4900 mTorr. It indicates the system requires less bias voltage at reduced pressures at various threshold shocks. Often MEMS devices are vacuum packaged and it is helpful to know the initial voltage required for the threshold shock of interest.

In summary, the proposed autonomous sensing device presents two tuning parameters for detecting shocks. At the triboelectric transducer, the user can adjust the shock voltage generation characteristics as well as the generator sensitivity by tuning the axial force p. At the electrostatic transducer, the

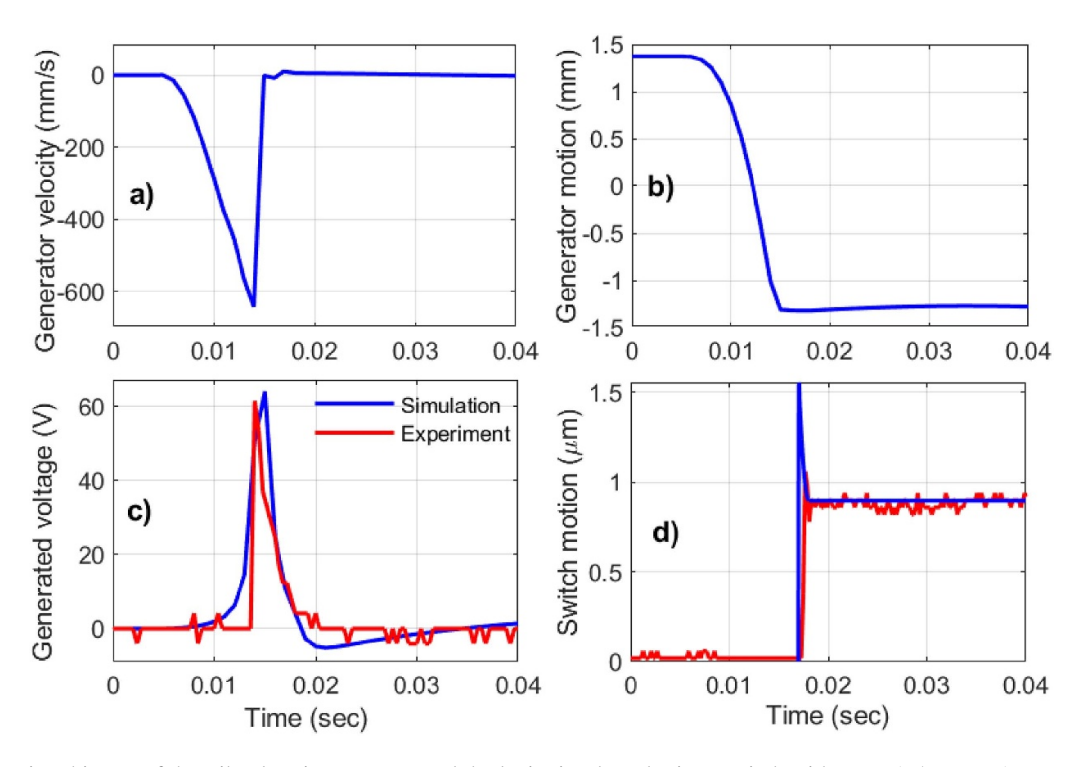


Figure 8. The Time history of the triboelectric generator and the levitation-based micro-switch with $V_b = 1.5$ V, P = 1 atm and actuated by the base-acceleration of a = 12g: (a) and (b) show the velocity and motion of the generator aluminum mass, respectively; (c) simulation and experimental results of the generated voltage; (d) simulation and experimental results of the switch displacement. The switch motion was measured by a laser vibrometer.

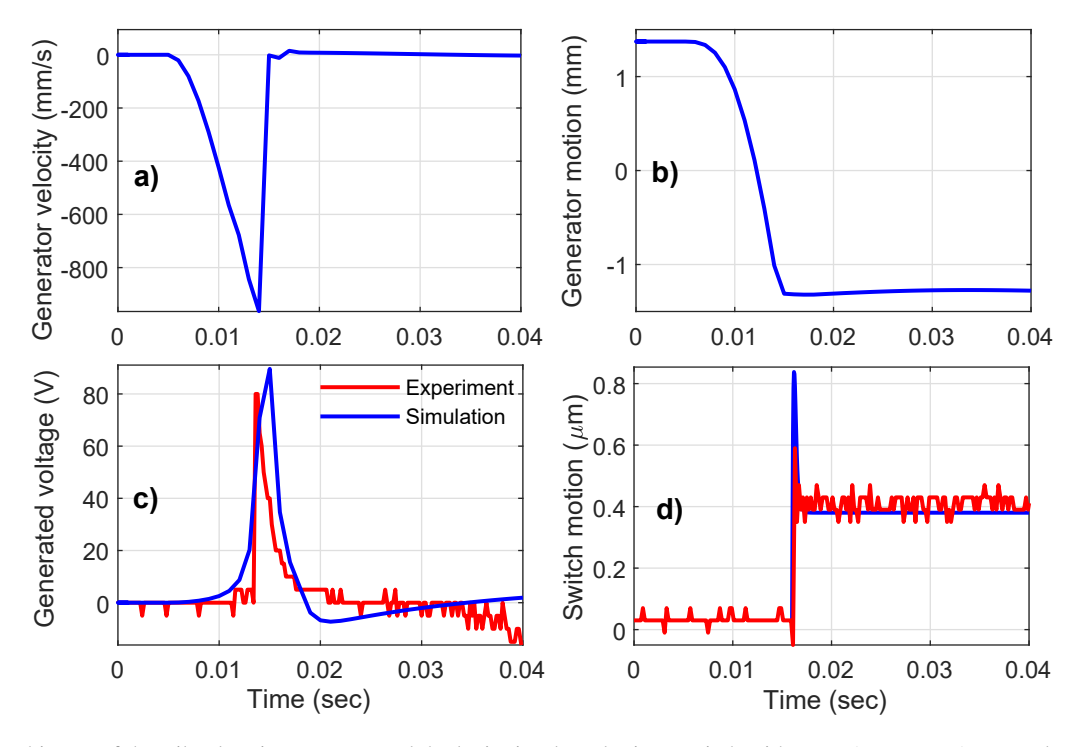


Figure 9. Time history of the triboelectric generator and the levitation-based micro-switch with $V_b = 1.7$ V, P = 1 atm and actuated by the base-acceleration of a = 20g: (a) and (b) show the generator velocity and displacement, respectively; (c) simulation and experimental results of the generated voltage; (d) Simulation and experimental results of the switch displacement. The switch motion was measured by a laser vibrometer.

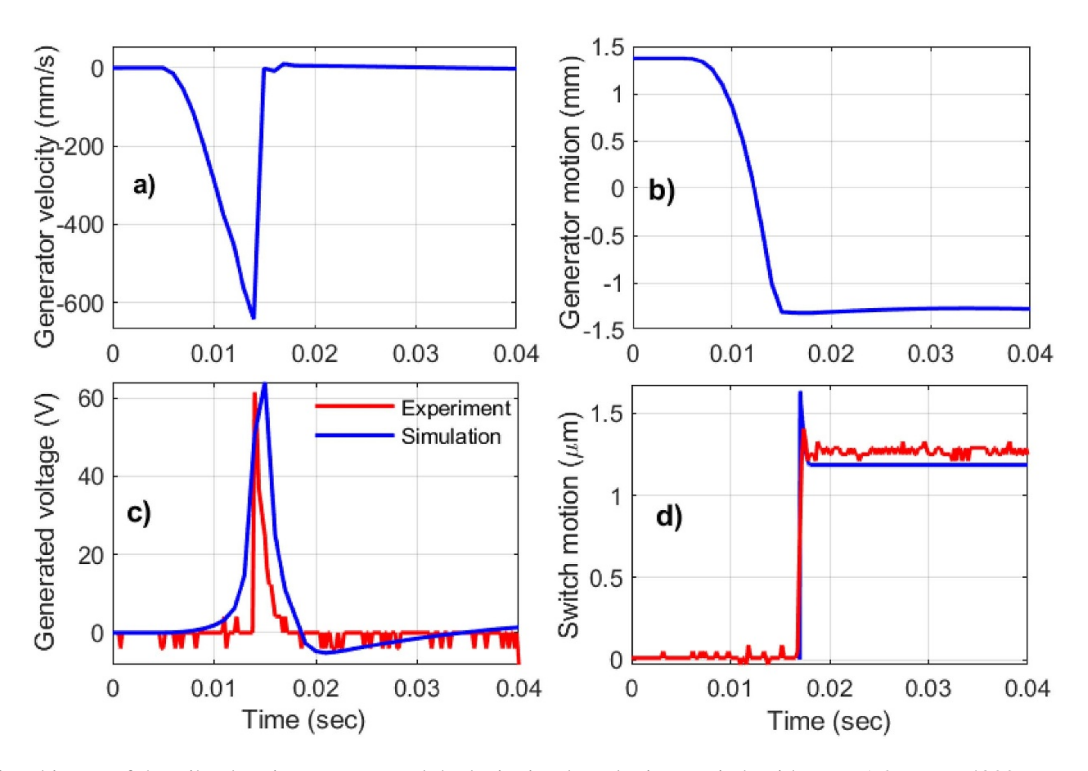


Figure 10. Time history of the triboelectric generator and the levitation-based micro-switch with $V_b = 1.2$ V, P = 4900 mTorr and actuated by the base-acceleration of a = 12g: (a) and (b) show the generator velocity and displacement, respectively; (c) simulation and experimental results of the generated voltage; (d) Simulation and experimental results of the switch displacement. The switch motion was measured by a laser vibrometer.

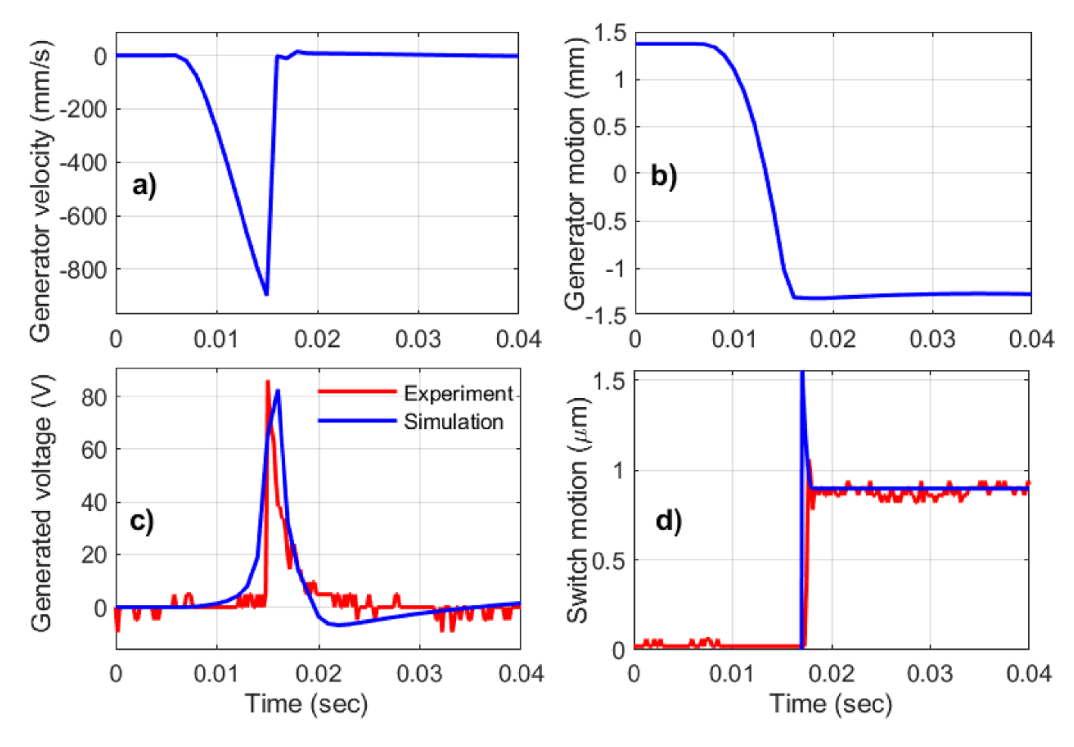


Figure 11. Time history of the triboelectric generator and the levitation-based micro-switch with $V_b = 1.4$ V, P = 4900 mTorr and actuated by the base-acceleration of a = 20g: (a) and (b) show the generator velocity and displacement, respectively; (c) simulation and experimental results of the generated voltage; (d) Simulation and experimental results of the switch displacement. The switch motion was measured by a laser vibrometer.

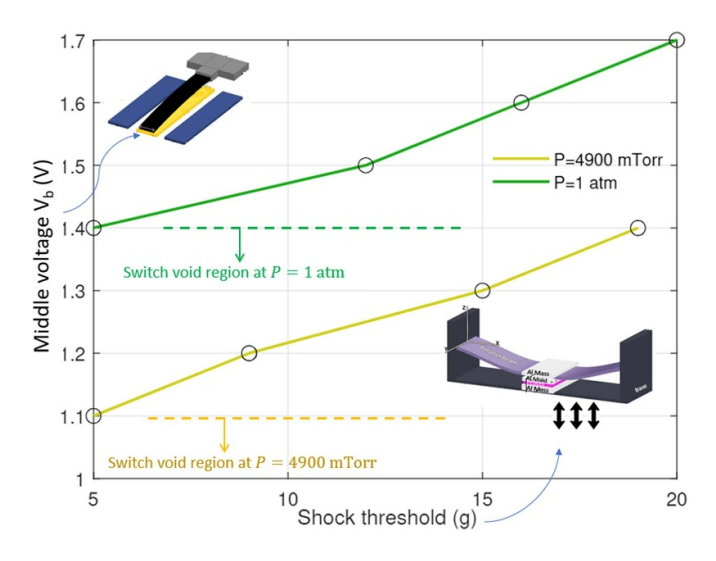


Figure 12. The micro-switch middle voltage governs the threshold shock of detection. This figure shows the experiments for how much middle voltage is required for achieving a specific shock threshold during a successful actuation process. The generator axial force is p = 30 N.

middle voltage of the micro-switch defines a threshold on the triggering process (disconnection process) that can adjust the threshold shock. Currently, the shock sensing system is applicable for 1-dimensional mechanical shocks. The generator can be improved in a way that it becomes sensitive to shocks in multiple directions. For future miniaturization of the system, the size of the bi-stable mechanism can be reduced. However, considering the amount of required voltage for the microswitch actuation (60–80 V), the area of the bi-stable generator cannot be reduced significantly because it fails to produce the sufficient voltage. One solution though can be enhancing the surface roughness of the dielectric layer that enables producing more voltage per area [45].

6. Conclusion

Three physical phenomena, electrostatic levitation, triboelectric generation and bi-stable structures are combined to present an autonomous shock sensing system. The recognition of the environmental shocks is followed by triggering a micro-switch as the shock power exceeds a tunable threshold. A bi-stable triboelectric generator detects and harvests the environmental shocks in one direction as a result of which a high-amplitude voltage is generated. The triggering part is a levitation-based normally-ON micro-switch that is disconnected by applying the generated voltage to its side electrodes. The integrated system is independent of any external power supply except a DC low voltage battery (\sim 1.5 V) for operation. By contrast with the current safety systems that mostly rely on control units, the proposed system is fully autonomous. This system is safe and provides a reliable mechanism as the user is not concerned with the errors in control systems. Both components of the system (triboelectric and electrostatic transducer) are tunable. The productivity of the bi-stable generator can be adjusted using the axial load. Moreover, the switch sensitivity can be adjusted by a small bias voltage that causes the initial pulled-in position.

Data availability statement

All data that support the findings of this study are included within the article (and any supplementary files).

Acknowledgment

The authors would like to acknowledge the financial support of this study by National Science Foundation (NSF) through Grant No. CMMI 1919608.

ORCID iDs

Mohammad Mousavi https://orcid.org/0000-0003-2410-4595

Shahrzad Towfighian https://orcid.org/0000-0002-5084-7395

References

- [1] Hsieh H H, Hsu F C and Chen Y F 2018 ACS Sensors 3 113-20
- [2] Lu D et al 2020 Adv. Healthcare Mater. 9 2000942
- [3] Bouchaala A, Jaber N, Shekhah O, Chernikova V, Eddaoudi M and Younis M I 2016 Appl. Phys. Lett. 109 013502
- [4] Marchal T, Philippe J, Henry D, De Paolis M V, Coustou A, Pons P and Aubert H 2019 Millimetre-wave interrogation of passive sensors embedded inside closed reverberant environments from dual-polarized passive repeaters 2019 49th European Microwave Conf. (EuMC) (IEEE) pp 33–36
- [5] Feng W, Friedt J M, Goavec-Merou G and Sato M 2018 IEEE Sensors J. 19 594–602
- [6] Yue X, Kauer M, Bellanger M, Beard O, Brownlow M, Gibson D, Clark C, MacGregor C and Song S 2017 IEEE Internet Things J. 4 2092–103
- [7] Suzuki K, Chee S and Morita T 2018 Self-sensing grasping with piezoelectric manipulator ACTUATOR 2018; 16th Int. Conf. on New Actuators (VDE) pp 1–3
- [8] Ma Y, Ji Q, Chen S and Song G 2017 J. Renew. Sustain. Energy 9 054702
- [9] Zhang Z, Kan J w, Wang S, Wang H, Ma J and Jiang Y 2016 J. Intell. Mater. Syst. Struct. 27 581–91
- [10] Demori M, Ferrari M, Bonzanini A, Poesio P and Ferrari V 2017 Sensors 17 2100
- [11] Rozgić D and Marković D 2017 IEEE Trans. Biomed. Circuits Syst. 11 773–83
- [12] Shi J et al 2019 Nanoscale 11 7513-19
- [13] Xie L, Chen X, Wen Z, Yang Y, Shi J, Chen C, Peng M, Liu Y and Sun X 2019 Nano-Micro Lett. 11 39
- [14] Pyo S, Kim M O, Kwon D S, Kim W, Yang J H, Cho H S, Lee J H and Kim J 2020 Smart Mater. Struct. 29 055026
- [15] Wu C et al 2019 Adv. Funct. Mater. 29 1901102
- [16] Chen C et al 2019 Nano Energy 62 442-8
- [17] Wang P et al 2018 Adv. Funct. Mater. 28 1705808
- [18] Haque R I and Briand D 2019 Smart Mater. Struct. 28 085002
- [19] Pu X, Guo H, Chen J, Wang X, Xi Y, Hu C and Wang Z L 2017 Sci. Adv. 3 e1700694
- [20] Huynh T P and Haick H 2018 Adv. Mater. 30 1802337
- [21] Fatma B, Gupta S, Chatterjee C, Bhunia R, Verma V and Garg A 2020 *J. Mater. Chem.* A **8** 15023–33
- [22] Nafari A and Sodano H 2017 Smart Mater. Struct. 27 015029

- [23] Ibrahim A, Jain M, Salman E, Willing R and Towfighian S 2019 Smart Mater. Struct. 28 025040
- [24] Hossain N A, Yamomo G G, Willing R and Towfighian S 2021 IEEE/ASME Trans. Mechatronics accepted (https://doi.org/ 10.1109/TMECH.2021.3049327)
- [25] Gilbert J M and Balouchi F 2008 Int. J. Autom. Comput. 5 334–47
- [26] Ibrahim A, Yamomo G, Willing R and Towfighian S 2021 Journal of Intelligent Material Systems and Structures 32 16–28
- [27] Pallay M, Ibrahim A I, Miles R N and Towfighian S 2019 Appl. Phys. Lett. 115 133503
- [28] Pallay M, Miles R N and Towfighian S 2019 *J. Appl. Phys.* **126** 014501
- [29] Lara-Castro M, Herrera-Amaya A, Escarola-Rosas M A, Vázquez-Toledo M, López-Huerta F, Aguilera-Cortés L A and Herrera-May A L 2017 Micromachines 8 203
- [30] Pustan M, Birleanu C, Dudescu C, Muller R and Baracu A 2018 Integrated thermally actuated MEMS switch with the signal line for the out-of-plane actuation 2018th Symp. on Design, Test, Integration & Packaging of MEMS and MOEMS (DTIP) (IEEE) pp 1–4
- [31] Torres D, Dooley S and Starman L A 2018 Large out-of-plane deflection MEMS actuators for optical applications *Multidisciplinary Digital Publishing Institute Proc.* vol 2 p 1072
- [32] Chang J, Holyoak M J, Kannell G K, Beacken M, Imboden M and Bishop D J 2018 J. Microelectromech. Syst. 27 1135–47

- [33] Pallay M, Daeichin M and Towfighian S 2017 *Nonlinear Dyn.* **89** 1525–38
- [34] Zamanzadeh M, Jafarsadeghi-Pournaki I and Ouakad H M 2020 Nonlinear Dyn. 100 1105–23
- [35] Ouakad H M and Sedighi H M 2019 Int. J. Non-Linear Mech. 110 44–57
- [36] Li H, Duan X, Li G, Oldham K R and Wang T D 2017 *Micromachines* 8 159
- [37] Ouakad H M and Najar F 2019 J. Vib. Acoust. 141 041010
- [38] Yan B, Yu N, Zhang L, Ma H, Wu C, Wang K and Zhou S 2020 Smart Mater. Struct. 29 025022
- [39] Hussein H, Khan F and Younis M I 2020 Smart Mater. Struct. **29** 075033
- [40] Barth J, Krevet B and Kohl M 2010 Smart Mater. Struct. 19 094004
- [41] Mousavi M, Alzgool M and Towfighian S 2021 Electrostatic levitation: an elegant method to control MEMS switching operation *Nonlinear Dynamics*
- [42] Nelson D, Ibrahim A and Towfighian S 2019 Sensors Actuators A 285 666–75
- [43] Mahmoud M, Abdel-Rahmany E, El-Saadany E and Mansour R 2009 Battery-less electrostatic micro-power generator 2009 2nd Microsystems and Nanoelectronics Research Conf. (IEEE) pp 29–32
- [44] Narimani A, Golnaraghi M and Jazar G N 2004 J. Vib. Control 10 1775–94
- [45] Fan F R, Lin L, Zhu G, Wu W, Zhang R and Wang Z L 2012 Nano Lett. 12 3109–14